Supplement of

Measurement Report: Elevated excess-NH_3 can promote the redox reaction to produce HONO: Insights from the COVID-19 pandemic

Xinyuan Zhang et al.

Correspondence to: Shenbo Wang (shbwang@zzu.edu.cn) and Ruiqin Zhang (rqzhang@zzu.edu.cn).

Text S1 Detailed description of the aerosol and gas monitor.

The atmospheric sample passes through a $PM_{2.5}$ cut-off head, and both particles and gases enter a wet rotating dissolution device for diffusion. Subsequently, the particles in the sample undergo hygroscopic growth and condensation in an aerosol supersaturated vapor generator, followed by collection and ion chromatographic analysis. The gases in the sample are oxidized by H_2O_2 in the dissolution device, absorbed into a liquid solvent, and then entered the gas sample collection chamber for ion chromatographic quantification. During this process, the sample is extracted through a liquid diffusion filter, where interfering acidic and alkaline gases are removed. To achieve high collection efficiency, the airflow containing loaded ions then enters an aerosol supersaturated collector until the particles can be injected into the ion chromatograph. The ion chromatography system utilizes either suppressor or non-suppressor conductivity detection methods for ion analysis. Before running the samples, the ion chromatograph system needs to be calibrated using standard solutions. By comparing the data obtained from the sample with the data obtained from known standard solutions, the identification and quantification of sample ions can be performed. The data acquisition system generates chromatograms, and the chromatography software further converts each peak in the chromatogram into sample concentrations and outputs the results.

QA/QC

The instrument undergoes daily checks and maintenance, which typically involve ensuring the stability of internal standard response and maintaining a relative error within ±10% between the measured and theoretical concentrations of the internal standard. The system's data acquisition and transmission are carefully examined, along with monitoring the instrument's status information and collected data. This includes checking parameters such as sampling flow rate, chromatographic column

pressure, column temperature, conductivity, target compound peak retention time, and peak width to ensure their normal functioning. Regular replacement of consumables used by the instrument is carried out at predetermined intervals and frequencies. Additionally, standard curve measurements and calibration are performed in each season to guarantee the accuracy of the instrument's data. Calibration curve verification should be performed at least once per quarter. A standard series containing at least 6 calibration points, including zero concentration, should be prepared using standard solutions. The concentration range of the calibration curve should be set according to the actual environmental concentration levels and determined by manual injection. The obtained calibration curve should have a linear correlation coefficient (r) of $\geqslant$0.995. If this requirement is not met, the rationality of the internal standard solution concentration settings should be checked. When key components such as the quantitative loop, chromatographic column, or suppressor are replaced, a new calibration curve should be promptly established. After establishing the new calibration curve, the sample sequence in the analysis software should be updated. The minimum detection limit is also determined as follows: 0.002 μg/m^3 (Cl^-), 0.081 μg/m^3 (NH_4^+), 0.02 μg/m^3 (NO_3^-), 0.06 μg/m^3 (SO_4^{2-}), 0.002 μg/m^3 (Na^+), 0.08 μg/m^3 (K^+), 0.06 μg/m^3 (Ca^{2+}) and 0.007 μg/m^3 (Mg^{2+}).

According to the research about the uncertainties in MARGA measurements, such as Song et al. used a 20% uncertainty for MARGA measurements(Song et al., 2018), while Rumsey et al. found an error of 10% for detecting SO_4^{2-}, NO_3^-, and HNO_3, and 15% for NH_3 and NH_4^+ (Rumsey et al., 2014), uncertainties of 20% are assumed for the detection of NH_3 and NH_4^+, while uncertainties of 10% are assumed for other components. Due to the complex conditions encountered during the actual sampling process, including variations in calibration slopes, sampling volumes, solvent concentrations, temperature, atmospheric pressure, and sampling flow rates at different sampling points, it is important to note that the assumed values mentioned above may not accurately reflect the actual situation.

Text S2 Detailed description of the NO_2、SO_2 and carbon analyzer.

The NO_2 analyzer utilized the chemiluminescence technique to measure the concentration of NO_2 in the air. This involved converting NO_2 to NO using a molybdenum converter, and then quantifying the NO concentration. The principle behind the SO_2 analyzer involved measuring the amount of ultraviolet light emitted during the decay of high-energy state SO_2. This emitted light was used to calculate the concentration of SO_2.

The carbon analyzer principle is primarily based on the NIOSH-5040 method, which involves analyzing the thermal optical transmittance of quartz filter samples. It employs a calibrated non-dispersive infrared sensor to detect the evolving carbon. Under controlled conditions with inert helium gas, carbon formed during a gradually increasing temperature gradient is referred to as OC, while carbon evolved under a mixture of 90% helium.

Text S3 The uncertainty analysis of HONO

The HONO monitoring method adopted in this study is the wet-flow diffusion tube method (WEDD) (cylindrical or parallel plate(C. Zellweger, 1999; Takeuchi M, 2013)) in the diffusion tube method (Denuder), which is a common method for measuring HONO in wet chemistry and has high absorption efficiency. The device adopts a vertical setting, through the diffusion tube, the air in the atmosphere is pulled upward from the bottom, and the absorbent liquid is transported to the top of the diffusion tube through the air pump. When flowing under the action of gravity, a thin absorbent liquid film will be generated on the inner surface of the tube by the tension. The absorbent liquid film will absorb HONO, and the solution at the bottom of the diffusion tube will be sucked out through the air pump. Then it is sent to the ion chromatography for analysis. The integration time of the sample mainly depends on

the running time of the ion chromatography, which is about 5-30 min(Takeuchi M, 2013; C. Zellweger, 1999). Based on the original, some scholars developed the flow injection-chemiluminescence method and used it together with WEDD for the measurement of HONO. Its principle is mainly based on the fact that nitrite collected in solution is oxidized by hydrogen peroxide to peroxy-nitrite under acidic conditions, light radiation occurs during the reaction process, and its chemiluminescence intensity is detected. The detection limit is about 0.03 μg/m^3, and the temporal resolution is reduced to 70s(Mikuska et al., 2008; Zhao, 2010). Wang et al.(Wang et al., 2023) showed that the system detection limits of HONO, HNO_3, and NO_3^- were 65 ppt, 65 ppt, and 45 ng/m^3, respectively. Previous work has shown that HONO observations measured with this AIM-IC system agree well with HONO observations measured with the stripped coil-UV/Weiss absorption photometer (SC-AP) system(VandenBoer et al., 2014).

Text S4 Calculation and analysis of HONO sources

Considering that there is NO photolysis at night, the P_{OH+ON} values at U-ZK and R-PY points were calculated based on the model simulation by Wang et al.(Wang et al., 2022), assuming that the concentration of OH in the gas phase reaction between NO and ·OH was 0.8×10^6 cm^{-3}. The heterogeneity of NO_2 on ground and aerosol surfaces should be shown to be a secondary source of HONO at night. The formula for calculating P_{ground} and $P_{aerosol}$ is as follows equation 7-10. During the epidemic period, P_{ground} decreases due to the decrease of NO_2 concentration, while $P_{aerosol}$ decreases slightly. That is, the decrease of P_{ground} dominated the decrease in the heterogeneous production of HONO.

$$P_{ground} = \frac{1}{8}\times C_{NO_2}\times\frac{1}{H}\times\gamma_{NO_2\rightarrow ground} \quad (1)$$

$$P_{aerosol} = \frac{1}{4} \times C_{NO_2} \times \frac{S_a}{V} \times \gamma_{NO_2 \rightarrow aerosol} \quad (2)$$

$$C_{NO_2} = \sqrt{\frac{8RT}{\pi M}} \quad (3)$$

$$\frac{S_g}{V} = \frac{2.2}{H} \quad (4)$$

Where C_{NO2} is the average molecular velocity of NO_2 molecule (m s^{-1}); R is the ideal gas constant; T is the temperature (K); M is the molecular weight of NO_2 (kg mol^{-1}); $\gamma_{NO2 \rightarrow ground}$ and $\gamma_{NO2 \rightarrow aerosol}$ is the absorption coefficient of NO_2 on the ground and aerosol surface, respectively.

Direct emission refers to the HONO that can be released directly into the atmosphere through combustion (such as vehicle and biomass combustion). Here we use the HONO/NO_x ratio to estimate HONO concentration, which is generally considered to be the vehicle emission factor(Kramer et al., 2020; Hao et al., 2020; Yu et al., 2022) for HONO. The calculation formula is as follows：

$$[HONO_{emi}] = 0.65\% \times [NO_x] \quad (5)$$

Where $[HONO_{emi}]$ and $[NO_x]$ represent the HONO concentration emitted by vehicles and the observed NO_x concentration, respectively. For the emission coefficient, we chose 0.65% to calculate(Kramer et al., 2020; Hao et al., 2020; Huang et al., 2017).

During the epidemic period, the direct emission of HONO at U-ZK and R-PY points decreased compared with that before the epidemic period, which was also related to the decrease of motor vehicle activities during the epidemic period.

The photosensitive polyphase reaction of NO_2 on the surface of the ground ($P_{ground + hv}$) and the surface of the aerosol ($P_{aerosol + hv}$), according to the research of Zhang et al.(Zhang et al., 2020a), the formula calculated in this paper is as follows：

$$P_{ground+hv} = \frac{1}{8} \times C_{NO_2} \times \frac{1}{H} \times \gamma_{NO_2 \rightarrow ground} \times \frac{light\ intensity}{400} \quad (6)$$

$$P_{aerosol+hv} = \frac{1}{4} \times C_{NO_2} \times \frac{S_a}{V} \times \gamma_{NO_2 \rightarrow aerosol} \times \frac{light\ intensity}{400} \quad (7)$$

where light intensity was simulated by its relationship with JNO_2.(HOFZUMAHAUS, 1992;Trebs et al., 2009)

The calculation of $P_{nitrate}$ based on nitrate concentration (NO_3^-) and nitrate photolysis rate ($J_{nitrate \rightarrow HONO}$) measured at $PM_{2.5}$:

$$P_{nitrate} = J_{nitrate \rightarrow HONO} \times [NO_3^-] \quad (8)$$

In this formula, $J_{nitrate \rightarrow HONO}$ needs to be simulated by normalized UV value. Bao et. al(Bao et al., 2018) found when the apex Angle is 0°, $J_{nitrate \rightarrow HONO}$ varies in the range of 1.22×10^{-5} to $4.84\times 10^{-4}s^{-1}$, with an average of $8.24\times 10^{-5}s^{-1}$.

The emission rate of HONO (E_{HONO}, ppbv h^{-1}) from soil was calculated based on the emission flux (F_{HONO}, $gm^{-2}\ s^{-1}$) and the PBL height (H, m) according to Liu et. al(Liu et al., 2020a; Liu et al., 2020b) and by using the following equation:

$$E_{HONO} = \frac{\alpha \bullet F_{HONO}}{H} \quad (9)$$

$$F_{HONO} = \frac{EI_{HONO}}{A} \quad (10)$$

where, α is the conversion factor ($\alpha = \frac{1\times10^9 \cdot 3600 \cdot R \cdot T}{M \cdot P} = \frac{2.99\times10^{13} \cdot T}{M \cdot P}$); M is the molecular weight (g mol^{-1}); T is the temperature (K) and P is the atmospheric pressure (Pa); EI_{HONO} is the emission inventory of HONO (g s^{-1}); A is the core area of the observation site (m^2).

The convergence of HONO at night includes homopolar memorization of HONO and OH ($L_{HONO+OH}$) and dry deposition (L_{dep}), which can be calculated by the following formula:

$$L_{HONO+OH} = k_{HONO+OH} \times [OH] \times [HONO] \quad (11)$$

$$L_{dep} = \frac{v_d \times [HONO]}{H} \quad (12)$$

where $k_{HONO+OH}$ is the second-order reaction rate constant of HONO and OH

(5.0×10^{-12} cm^{-3} s^{-1}); υ_d is the dry deposition speed of HONO second-order reaction, with the empirical value of 0.02 m s^{-1}; and H is the effective mixing height of HONO, which is assumed to be 1000 m during daytime budget analysis(Gu et al., 2020; Xuan et al., 2023).

L_{photo} is calculated by the following formula:

$$L_{photo} = J_{HONO} \times [HONO] \quad (13)$$

Where J_{HONO} is the photolysis rate of HONO in this equation.

Text S5 Estimation of HONO formation rate

The redox reaction of NO_2 with SO_2 (R_1) is considered a crucial potential source of high concentrations of HONO in Northern China (Wang et al., 2016b; Cheng, 2016):

$$S(IV) + 2NO_2 + H_2O \rightarrow S(IV) + 2H^+ + 2NO_2^- \quad (R_1)$$

The rate expression for the reaction was estimated to:

$$d[S(VI)]/dt = k_1[NO_2][S(VI)], \quad (14)$$

where the $k_1 = (1.4\times10^5 + 1.24\times10^7)/2$ $M^{-1}s^{-1}$ for the pH range < 5;

$k_1 = (23.25\times(pH–5) + 1.4 + 124)/2\times10^5$ $M^{-1}s^{-1}$ for the pH range 5 < pH < 5.3;

$k_1 = (23.25\times(pH–5) + 1.4 + 12.6\times(pH–5.3) + 124)/2\times10^5$ $M^{-1}s^{-1}$ for the pH range 5.3 < pH < 5.8;

$k_1 = (12.6\times(pH–5.3) + 124+20)/2\times10^5$ $M^{-1}s^{-1}$ for the pH range 5.8 < pH < 8.7;

and $k_1 = (2\times10^6 + 1.67\times10^7)/2$ $M^{-1}s^{-1}$ for the pH range pH > 8.7. (Seinfeld et al., 1998)

In the above calculation formulas, the concentration of gas in the liquid is determined by Henry's constant (H^*). The calculation formula is in Table S2. SO_2 has a dissociation equilibrium in the solution, producing HSO_3^- and SO_3^{2-}. The ionization constants (K) are shown in the following Table S3. The H* and K are temperature-dependent. The values are given in Table S2 and S3 under the condition of 298K, converted to the value under the actual temperature using the following calculation formula:

$$H(T)\text{or } K(T) = H(T_{298K})\text{or}K(T_{298K})\exp\left[-\frac{\Delta H_{298K}}{R}\left(\frac{1}{T}-\frac{1}{298K}\right)\right] \quad (15)$$

Where $H(T)$、$K(T)$、$H(T_{298K})$, and $K(T_{298K})$ represent the H* and K at actual temperature and 298 K, respectively.

Influences of ionic strength on R_1 were not considered because of the high values predicted by the ISORROPIA-II model during the sampling periods (Cheng et al.,

2016). To evaluate the effects of mass transport, the formulation of a standard resistance model was adopted:

$$\frac{1}{R_{H,aq}} = \frac{1}{R_{aq}} + \frac{1}{J_{aq,lim}} \quad (16)$$

Where $R_{H,aq}$ is the sulfate production rate, R_{aq} is the aqueous-phase reaction rate, and $J_{aq,lim}$ is the limiting mass transfer rate. which could be calculated by the formulas as follows:

$$J_{aq,lim} = \min\{J_{aq}(SO_2), J_{aq}(X)\} \quad (17)$$

$$J_{aq}(X) = k_{MT}(X)\cdot[X] \quad (18)$$

Where [X] refers to the aqueous-phase concentrations of SO_2 or the oxidants O_{xi} calculated by the equation in Table S2. The mass transfer rate coefficient $k_{MT}(X)$ (s^{-1}) can be calculated by:

$$k_{MT} = [\frac{R_p^2}{3D_g} + \frac{4R_p}{3\alpha\nu}]^{-1} \quad (19)$$

Where R_p is the aerosol radius, D_g is the gas-phase molecular diffusion coefficient (0.2 $cm^2\ s^{-1}$ at 293K), v is the mean molecular speed of X (3×10^4 cm s^{-1}), and a is the mass accommodation of X on the droplet surface, and we adopted values of 0.11 and $2E^{-4}$ for SO_2 and NO_2, respectively referring to Cheng et al. (Cheng, 2016).

Figures

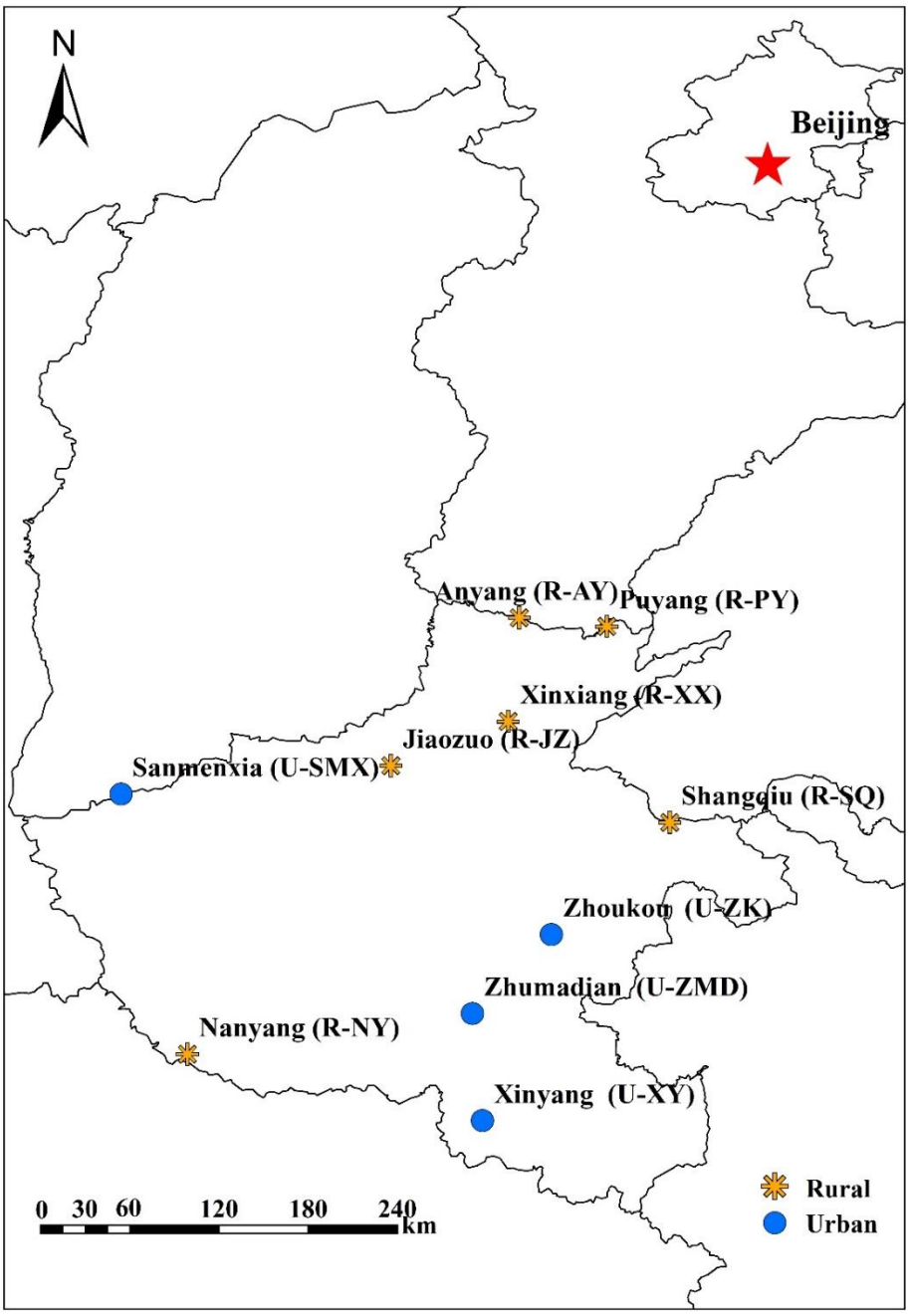

Figure S1. Sampling point map in Henan Province, China. © 2019 National Geomatics Center of China. (i.e., urban sites at Sanmenxia (U-SMX), Zhoukou (U-ZK), Zhuamdian (U-ZMD) and Xinyang (U-XY), rural sites at Anyang (R-AY), Xinxiang (R-XX), Puyang (R-PY)), Jiaozuo(R-JZ), Shangqiu (R-SQ) and Nanyang (R-NY). All rights reserved.

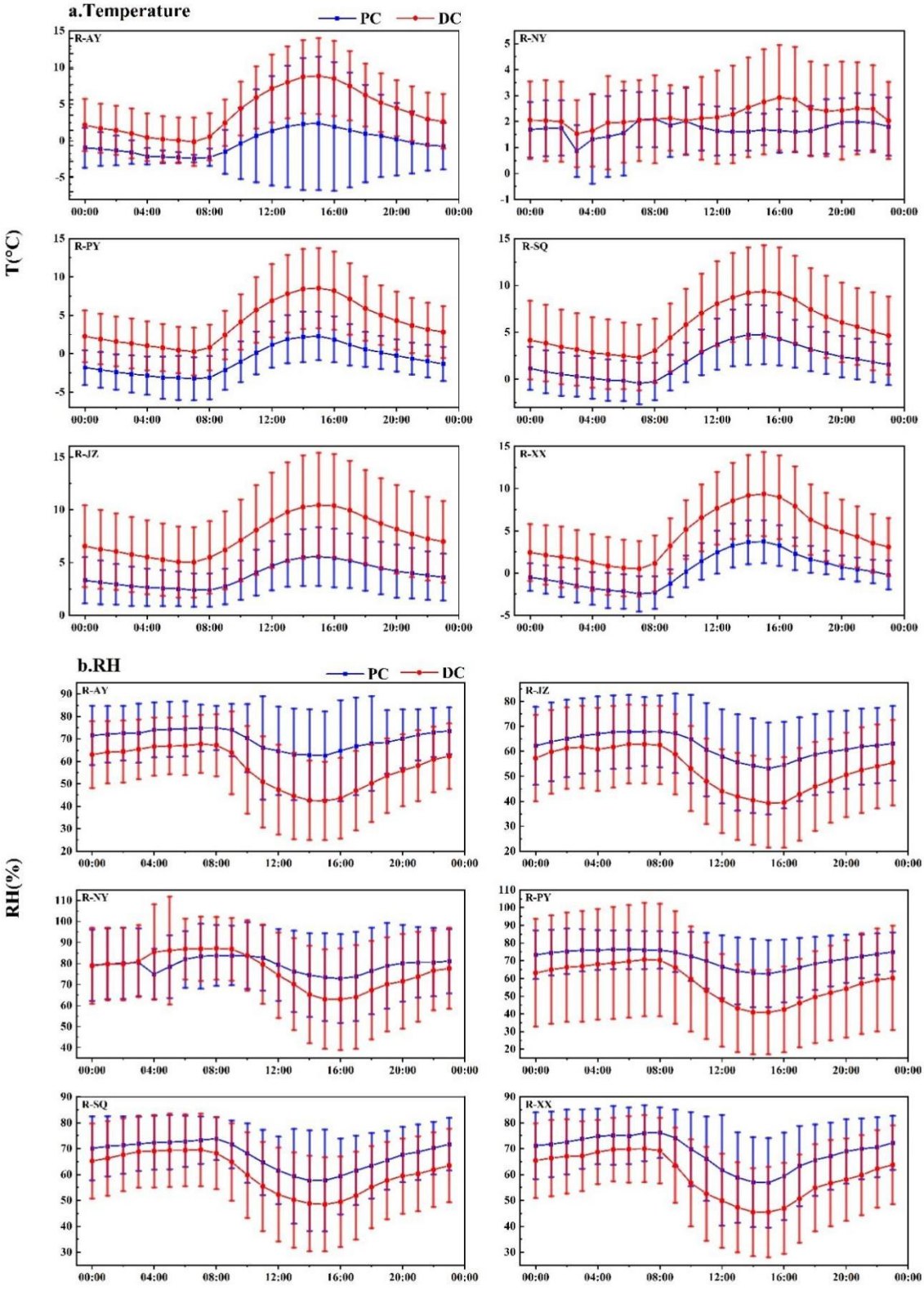

Figure S2. Daily changes in temperature and relative humidity (RH) in rural sites before (PC) and during (DC) the COVID-19 outbreak, the error bar represents the standard deviation. The upper and lower whiskers represent the standard deviation.

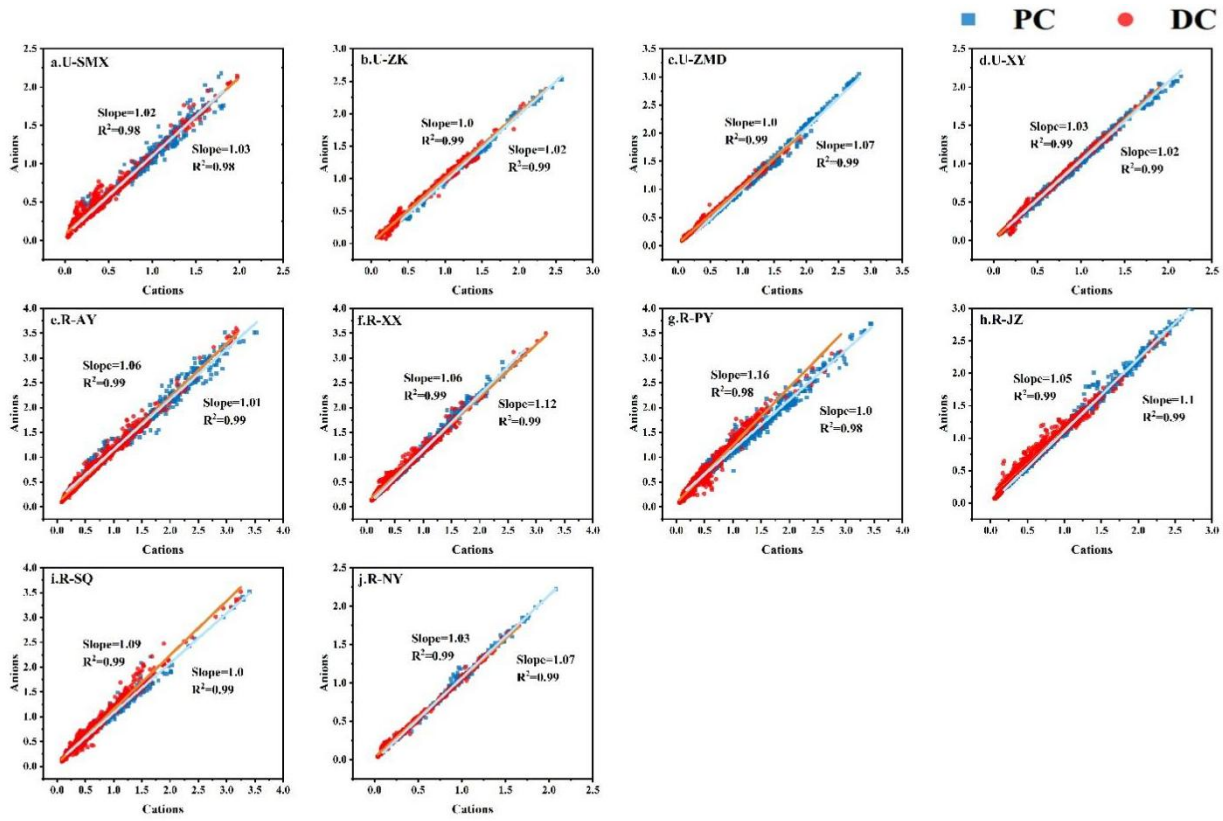

222

223 **Figure S3.** The equilibrium state of anions and cations at ten sites before (PC) and during

224 (DC) the COVID-19 outbreak.

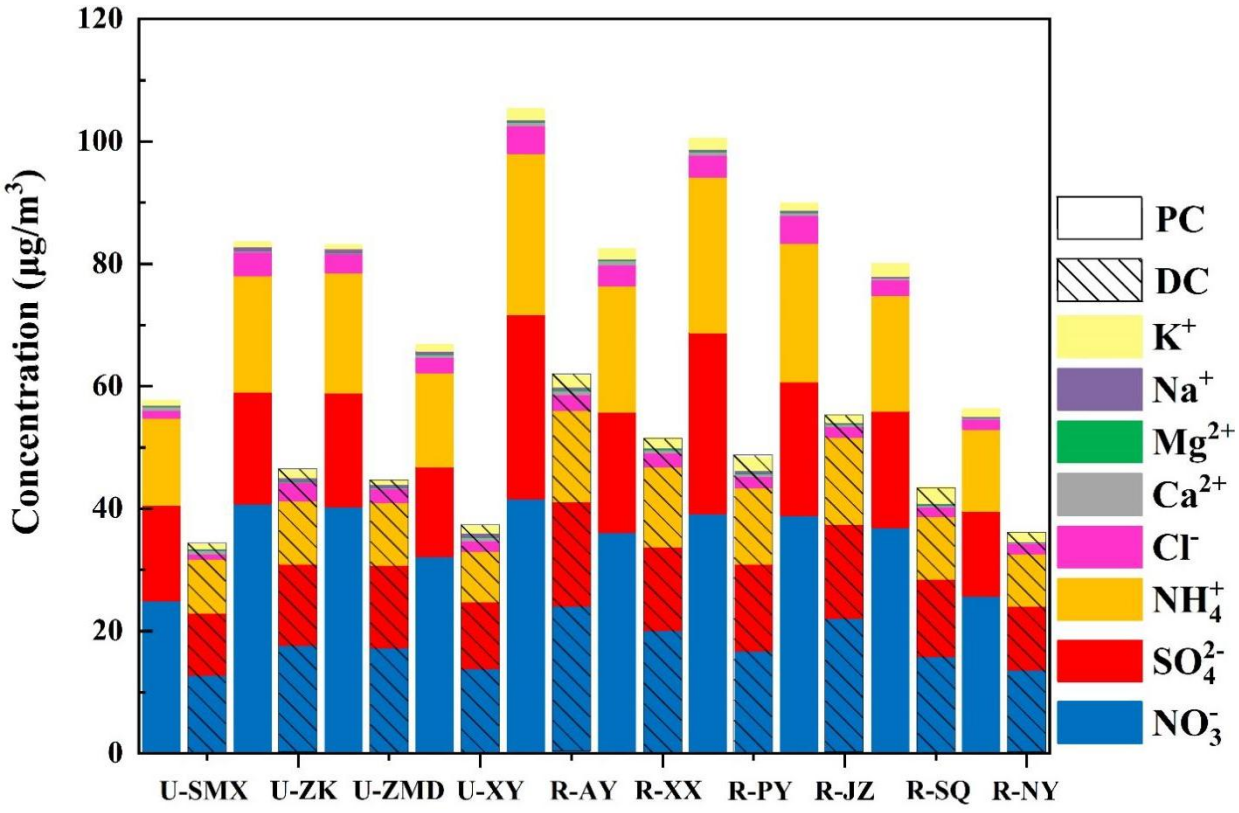

225

226

227 **Figure S4.** Concentrations of the water-soluble ions at the ten sites before (PC)

228 and during (DC) the COVID-19 outbreak.

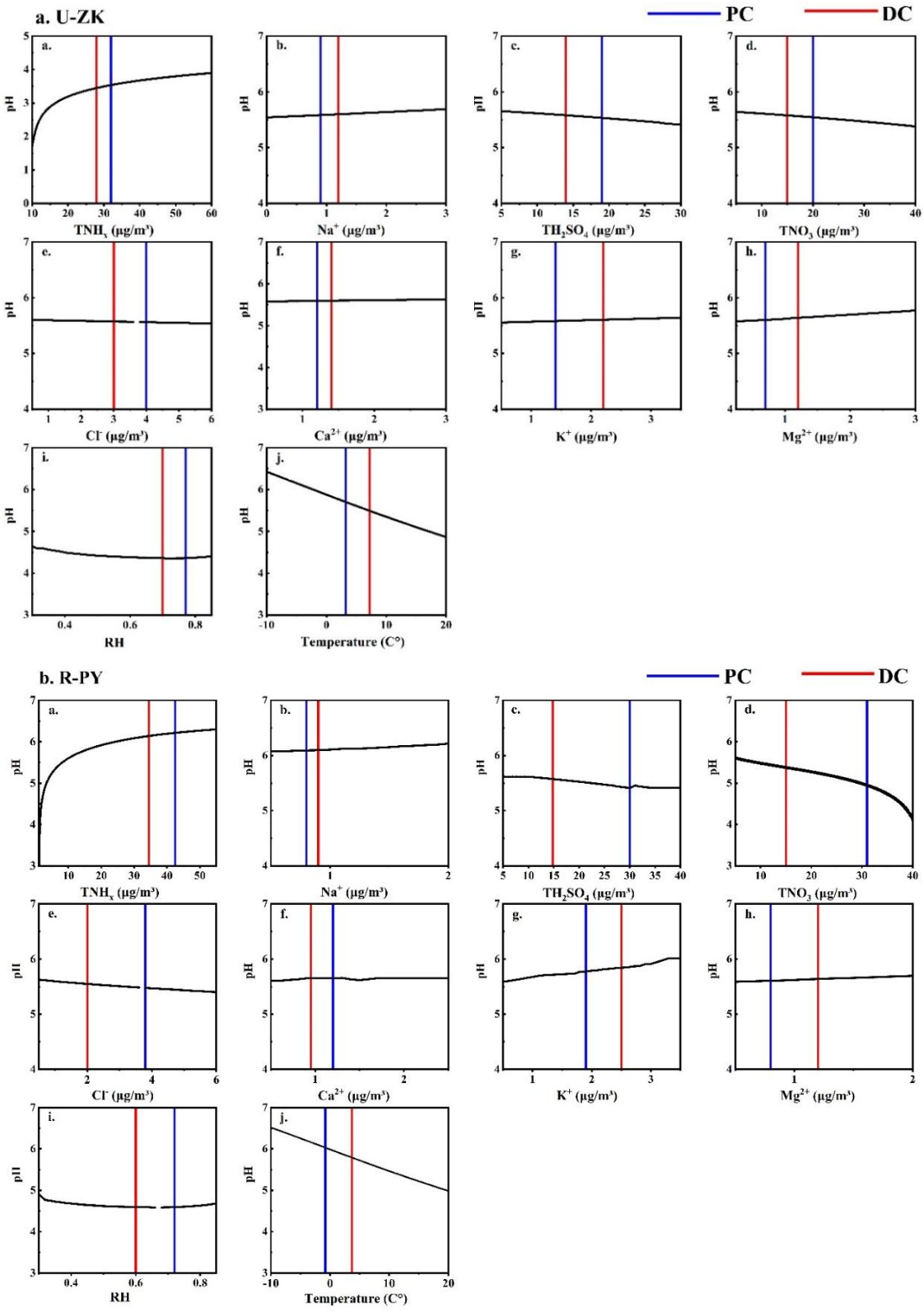

Figure S5. Sensitivity tests of pH to each factor. The vertical bar represents the mean values before (PC) and during (DC) the COVID-19 outbreak. The real-time measured values of a variable and the average values of other parameters were input into the ISORROPIA II model.

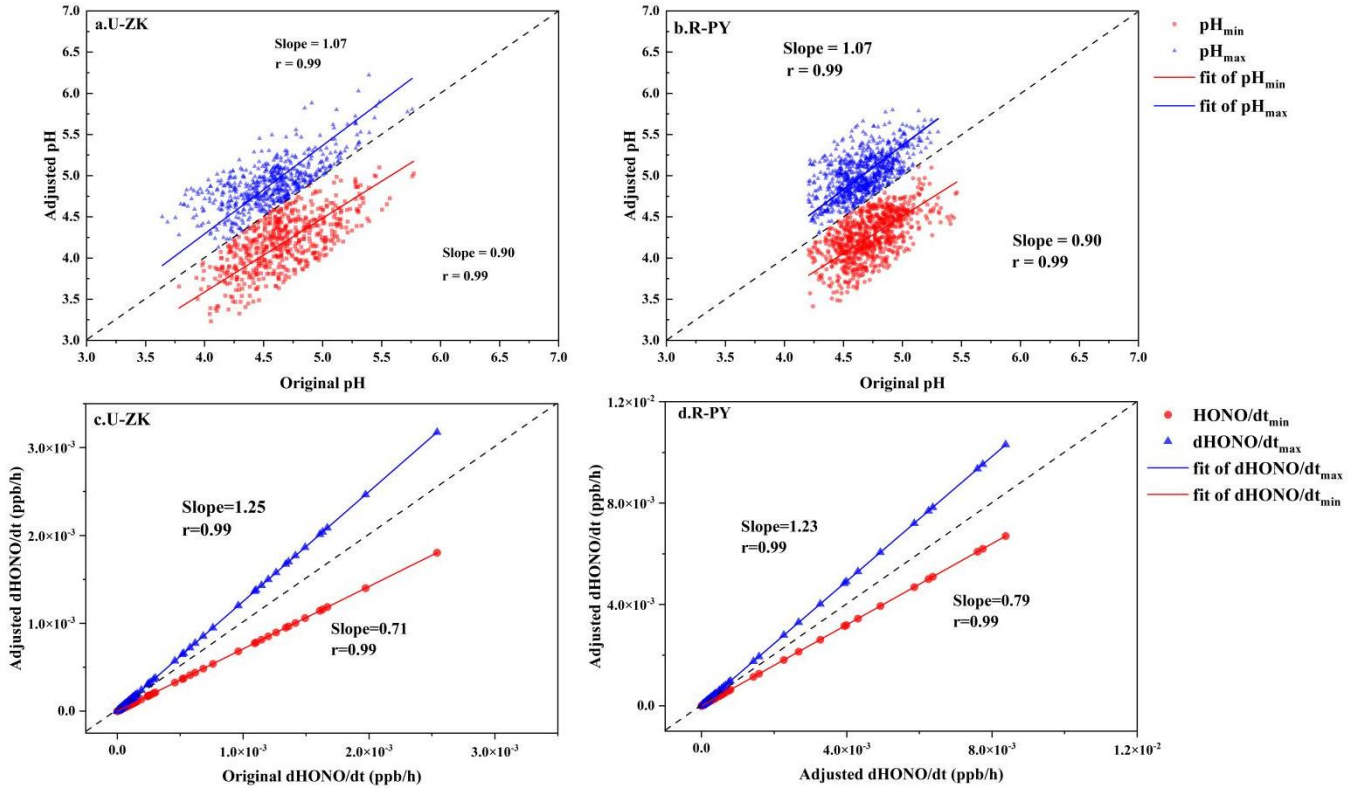

Figure S6. pH and R_1 uncertainties at the U-ZK and R-PY sites are based on two extreme scenarios of sensitivity to measurement uncertainty.

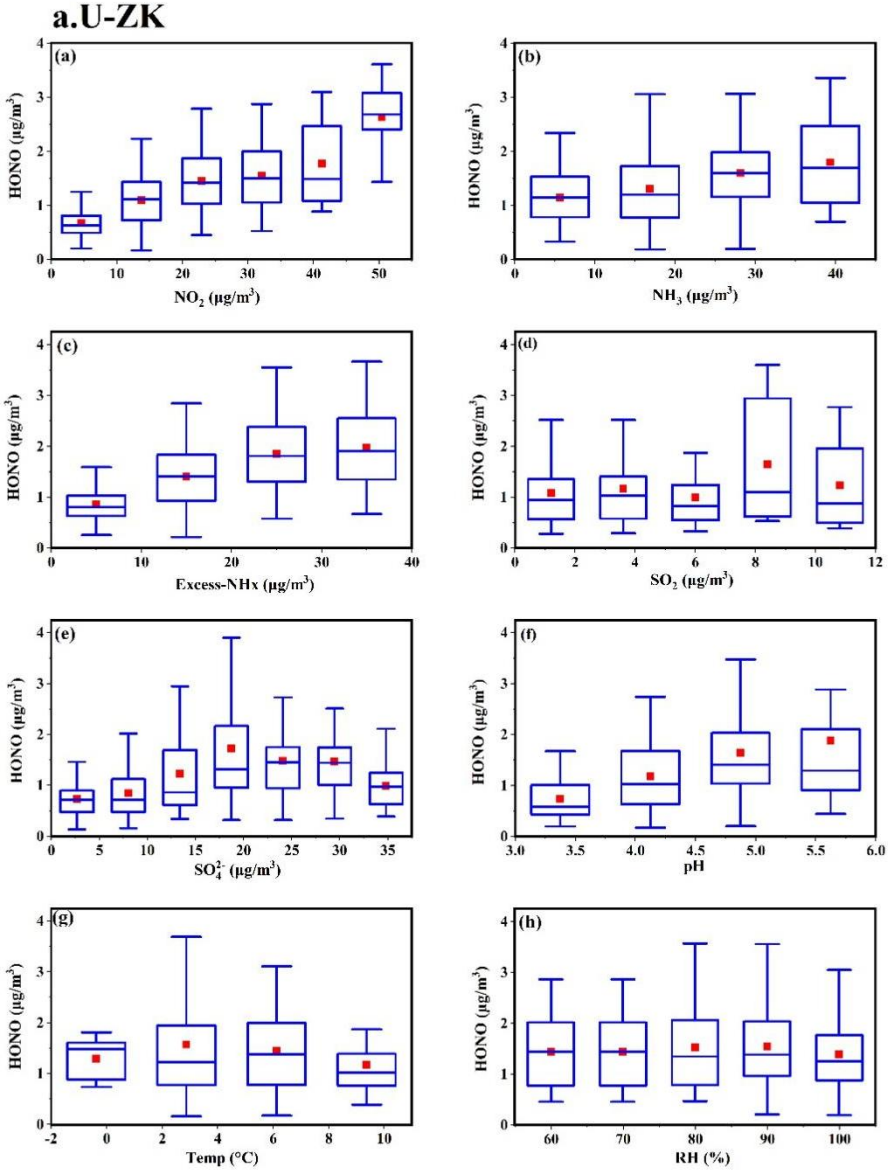
a.U-ZK
(a)
HONO (μg/m³)
NO₂ (μg/m³)
(b)
NH₃ (μg/m³)
(c)
Excess-NHx (μg/m³)
(d)
SO₂ (μg/m³)
(e)
SO₄²⁻ (μg/m³)
(f)
pH
(g)
Temp (°C)
(h)
RH (%)

240

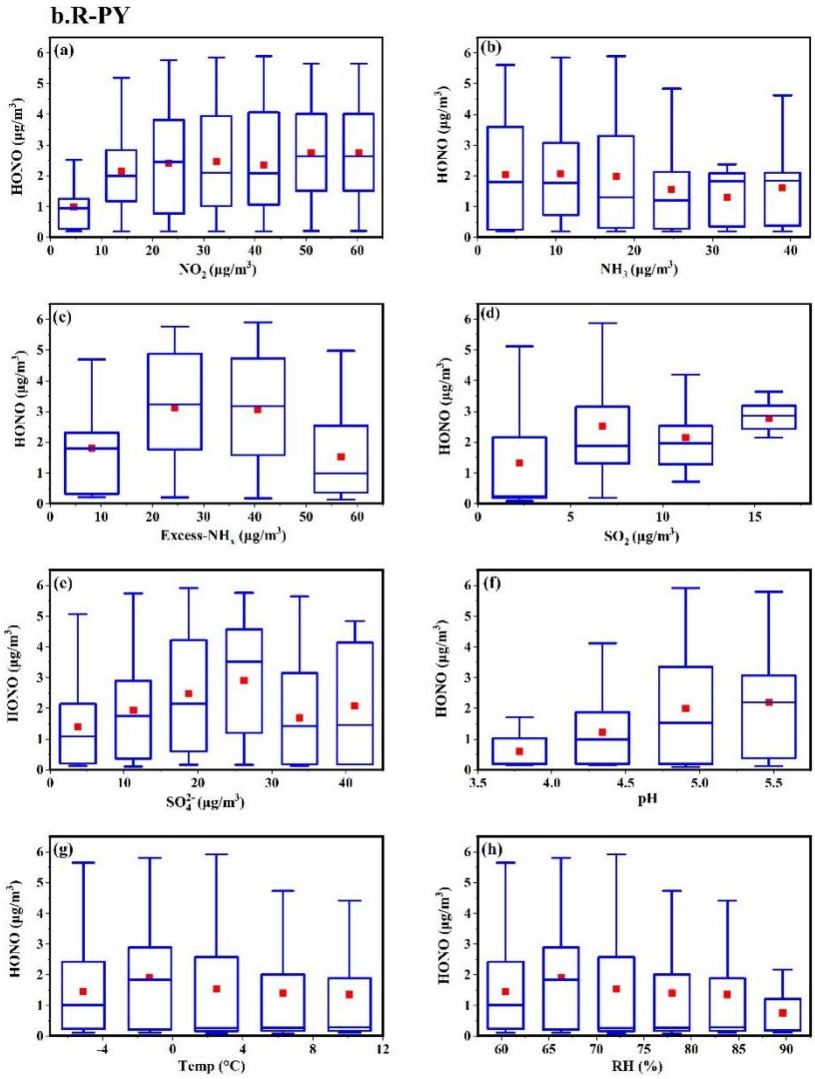

Figure S7. Relationship between HONO and main influencing factors during (DC) the COVID-19 outbreak at U-ZK and R-PY sites. Mean (red square), median (middle horizontal line), 25th and 75th percentiles (P25-P75, box), 10th and 90th percentiles (P10-P90, whiskers).

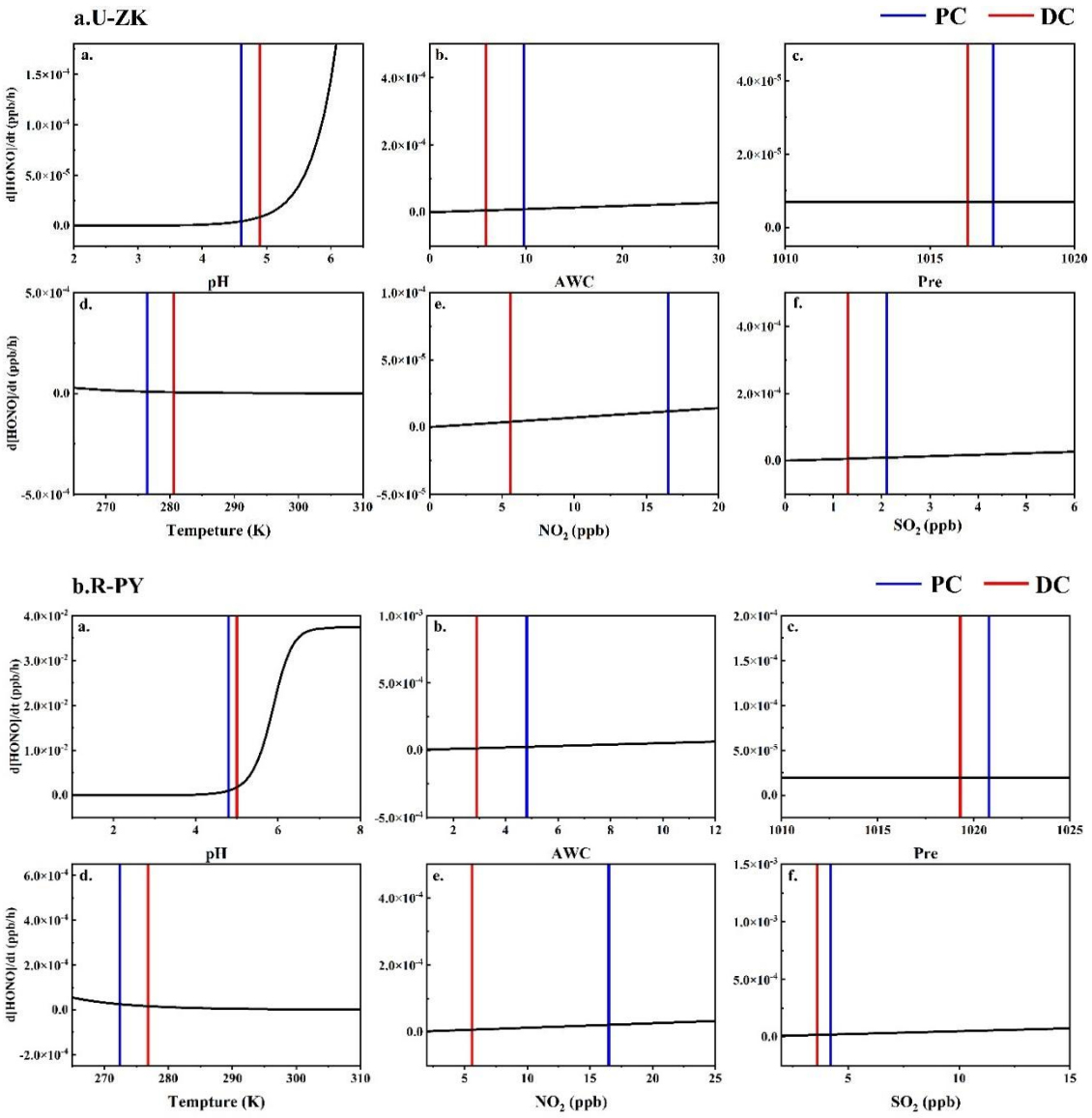

Figure S8. Sensitivity of HONO product rate to each factor. The vertical bar represents the mean values before (PC) and during (DC) the COVID-19 outbreak. The real-time measured values of a variable and the average values of other parameters were input into the production rate of R_1 reaction.

252 **Tables**

253 **Table S1.** Descriptions of the ten sampling sites in Henan Province, China.

Observation sites	Classifications	Abbreviations	Coordinates	Locations	Surrounding environment
Sanmenxia	Urban site	U-SMX	34.79 °N, 111.16 °E	Sanmenxia Environmental Protection Bureau	Roads, residential areas
Zhoukou	Urban site	U-ZK	33.65° N, 114.65° E	Chuanhui District People's Government	Roads, residential areas
Zhumadian	Urban site	U-ZMD	33.01° N, 114.01° E	Huanghuai College	Roads, residential areas, shopping malls
Xinyang	Urban site	U-XY	32.14° N, 114.09° E	Xinyang Museum	Roads, residential areas, shopping malls
Anyang	Rural site	R-AY	36.22°N, 114.39° E	Baizhuang Town Xindian North Street China Resources Gas (Andan Station)	Highways, villages, farmland
Xinxiang	Rural site	R-XX	35.38° N, 114.30° E	Banzao Township Central School in Yanjin County	Villages, farmland
Puyang	Rural site	R-PY	36.15° N, 115.10° E	Nanle County Longwang Temple Station	Villages, farmland
Jiaozuo	Rural site	R-JZ	35.02° N, 113.35° E	The Second River Bureau of Jiefeng Village, Beiguo Township, Wuxi County	Villages, farmland
Shangqiu	Rural site	R-SQ	34.56° N, 115.61° E	Liangyuan Huanghe Gudao National Forest Park	Highways, villages, farmland
Nanyang	Rural site	R-NY	32.68° N, 111.70° E	Nanyang Tangshan Park	Villages, farmland

254

255 **Table S2.** Constants for calculating the apparent Henry's constant (H*).

Equilibrium	H ($M\ atm^{-1}$) at 298K	$-\triangle H_{298K}/R$ (K)
$SO_2(g) \leftrightarrow SO_2(aq)$	1.23	3145.3
$NO_2(g) \leftrightarrow NO_2(aq)$	1.00E-02	2516.2

256

257 **Table S3.** Constants for calculating the ionization constants (K).

Equilibrium	K (M) at 298K	$-\triangle H_{298K}/R$ (K)
$SO_2 \cdot H_2O \leftrightarrow H^+ + HSO_3^-$	1.30E-02	1960
$HSO_3^- \leftrightarrow H^+ + SO_3^{2-}$	6.60E-08	1500

258

259 **Table S4.** Comparisons of NH_3 concentrations (mean ± standard deviation) (μg/m^3)
260 from studies in other cities.
261

Sampling sites	Seasons	Years	NH_3 (μg/m^3)	Sites	References
Delhi, India	Winter	2013–2015	19.2 ± 3.5	Urban	[(Saraswati et al., 2019)]
Osaka, Japan	Winter	2015	1.5 ± 0.7	Urban	[(Huy et al., 2017)]
Toronto, Canada	Winter	2007	0.8 ± 0.5	Urban	[(Hu et al., 2014)]
Kanpur, India	Winter	2007	21.7 ± 5.8	Urban	[(Behera and Sharma, 2010)]
Nanjing	Winter	2014	6.7	Urban	[(Wang et al., 2016b)]
Yangtze River Delta	Winter	2019	9.3 ± 4.0	Urban	[(Wang et al., 2021)]
Shanghai	Winter	2014	2.8 ± 1.0	Urban	[(Wang et al., 2018)]
Tianjin	Winter	2015	12.0	Urban	[(Shi et al., 2019)]
Xi'an	Winter	2012	17.5 ± 9.1	Urban	[(Wang et al., 2016a)]
Fujian	Winter	2016	12.8 ± 4.8	Urban	[(Wu et al., 2017)]
Beijing	Winter	2015	15.1 ± 2.9	Urban	[(Wang et al., 2016a)]
Beijing	Winter	2017	13.1 ± 1.6	Urban	[(Zhang et al., 2020b)]
Beijing	Winter	2020	19.9 ± 3.8	Urban	[(Zhang et al., 2020b)]
Taoyuan	Winter	2017–2018	1.7 ± 1.9	Urban	[(Duan et al., 2021)]
Zhengzhou	Winter	2018	19.0 ± 4.0	Rural	[(Wang et al., 2020)]
Quzhou	Winter	2019	29.5 ± 2.2	Rural	[(Feng et al., 2022)]
Gucheng	Winter	2016	9.3	Rural	[(Xu et al., 2019)]
Chongming	Winter	2019–2020	9.3 ± 4.0	Rural	[(Lv et al., 2022)]
Shanglan	Winter	2017–2018	2.5 ± 2.6	Rural	[(Duan et al., 2021)]

Table S5. The concentration (mean ± standard deviation) of relative humidity (RH), temperature (T), $\varepsilon(NH_4^+)$ at the ten sites before (PC) and during (DC) the COVID-19 outbreak.

Sites	Substances	Total	PC	DC
U-SMX	RH (%)	54.8 ± 18.0	60.6 ± 16.5	51.2 ± 18.0
	T (℃)	5.6 ± 4.2	3.1 ± 2.1	7.0 ± 4.4
	$\varepsilon(NH_4^+)$	0.43 ± 0.20	0.54 ± 0.18	0.36 ± 0.18
U-ZK	RH (%)	70.1 ± 21.9	73.6 ± 14.5	69.4 ± 22.4
	T (℃)	6.4 ± 4.3	3.8 ± 2.3	7.0 ± 4.5
	$\varepsilon(NH_4^+)$	0.43 ± 0.20	0.59 ± 0.14	0.32 ± 0.17
U-ZMD	RH (%)	74.9 ± 23.3	84.4 ± 17.8	68.9 ± 24.4
	T (℃)	5.6 ± 4.6	2.9 ± 2.7	7.4 ± 4.8
	$\varepsilon(NH_4^+)$	0.48 ± 0.21	0.62 ± 0.17	0.38 ± 0.18
U-XY	RH (%)	77.0 ± 22.1	86.7 ± 13.3	74.3 ± 23.3
	T (℃)	7.7 ± 4.5	4.7 ± 2.2	8.5 ± 4.6
	$\varepsilon(NH_4^+)$	0.55 ± 0.21	0.71 ± 0.14	0.45 ± 0.18
R-AY	RH (%)	62.2 ± 17.9	70.1 ± 14.9	57.2 ± 17.8
	T (℃)	2.6 ± 0.9	-0.2 ± 2.5	4.4 ± 4.7
	$\varepsilon(NH_4^+)$	0.46 ± 0.17	0.57 ± 0.15	0.39 ± 0.14
R-XX	RH (%)	63.0 ± 17.0	68.7 ± 14.6	59.5 ± 17.5
	T (℃)	2.9 ± 4.6	0.3 ± 2.8	4.4 ± 4.8
	$\varepsilon(NH_4^+)$	0.40 ± 0.17	0.52 ± 0.16	0.35 ± 0.14
R-PY	RH (%)	63.6 ± 18.0	71.5 ± 14.6	57.6 ± 18.0
	T (℃)	1.7 ± 4.8	-0.8 ± 3.2	3.6 ± 4.9
	$\varepsilon(NH_4^+)$	0.43 ± 0.17	0.58 ± 0.13	0.34 ± 0.13
R-JZ	RH (%)	56.3 ± 18.5	62.0 ± 16.7	52.8 ± 18.7
	T (℃)	4.1 ± 4.4	1.7 ± 2.6	5.6 ± 4.7
	$\varepsilon(NH_4^+)$	0.37 ± 0.14	0.46 ± 0.13	0.32 ± 0.13
R-SQ	RH (%)	63.2 ± 15.6	67.5 ± 12.6	60.5 ± 17.0
	T (℃)	4.2 ± 4.5	2.0 ± 2.9	5.6 ± 4.7
	$\varepsilon(NH_4^+)$	0.45 ± 0.19	0.63 ± 0.12	0.35 ± 0.14
R-NY	RH (%)	75.9 ± 19.1	79.3 ± 17.7	73.9 ± 19.6
	T (℃)	5.7 ± 3.8	3.6 ± 2.6	6.9 ± 3.9
	$\varepsilon(NH_4^+)$	0.59 ± 0.19	0.73 ± 0.12	0.52 ± 0.18

Table S6. The concentration (mean ± standard deviation) of required ammonia (Required-NH_x) and excess ammonia (Excess-NH_x) at the ten sites before (PC) and during (DC) the COVID-19 outbreak.

Sites	Substances	Total (μg/m³)	PC (μg/m³)	DC (μg/m³)
U-SMX	Required-NH_4^+	9.1 ± 7.1	12.7 ± 7.1	7.0 ± 6.2
	Excess-NH_4^+	14.7 ± 11.2	13.6 ± 10.4	15.3 ± 11.6
U-ZK	Required-NH_4^+	15.2 ± 9.6	21.4 ± 8.6	11.6 ± 8.4
	Excess-NH_4^+	14.6 ± 8.3	11.9 ± 6.0	16.1 ± 9.0
U-ZMD	Required-NH_4^+	13.9 ± 9.8	19.4 ± 9.8	10.4 ± 8.0
	Excess-NH_4^+	12.8 ± 8.7	11.6 ± 8.2	13.6 ± 8.8
U-XY	Required-NH_4^+	10.2 ± 7.5	14.6 ± 7.3	7.4 ± 6.2
	Excess-NH_4^+	7.8 ± 4.6	6.5 ± 4.4	8.7 ± 4.5
R-AY	Required-NH_4^+	17.1 ± 12.4	23.9 ± 13.4	12.8 ± 9.5
	Excess-NH_4^+	21.2 ± 9.4	20.2 ± 9.2	21.9 ± 9.4
R-XX	Required-NH_4^+	13.5 ± 9.6	18.0 ± 9.8	10.7 ± 8.2
	Excess-NH_4^+	23.3 ± 11.4	19.6 ± 10.8	25.6 ± 11.2
R-PY	Required-NH_4^+	13.8 ± 11.0	22.1 ± 12.5	9.3 ± 6.6
	Excess-NH_4^+	22.3 ± 10.8	17.5 ± 8.6	25.0 ± 11.0
R-JZ	Required-NH_4^+	15.4 ± 10.4	20.3 ± 10.6	12.5 ± 9.1
	Excess-NH_4^+	27.5 ± 12.9	26.0 ± 13.1	28.4 ± 12.7
R-SQ	Required-NH_4^+	13.2 ± 9.1	19.1 ± 8.9	9.9 ± 7.3
	Excess-NH_4^+	15.1 ± 8.6	10.1 ± 5.4	17.9 ± 8.7
R-NY	Required-NH_4^+	9.9 ± 6.6	13.0 ± 6.9	8.1 ± 5.8
	Excess-NH_4^+	6.0 ± 3.6	4.4 ± 3.3	6.9 ± 3.4

Table S7. Comparison of the particle pH values in this study (mean ± standard) deviation during the COVID-19 outbreak (DC) and other sites (mean or mean ± standard).

	Observation Sites	Periods	pH	References
Urban	Sanmenxia	Jan–Feb 2020	4.8 ± 0.9	This study (DC)
	Zhoukou	Jan–Feb 2020	5.1 ± 0.4	
	Zhumadian	Jan–Feb 2020	4.8 ± 1.2	
	Xinyang	Jan–Feb 2020	4.6 ± 1.3	
Rural	Anyang	Jan–Feb 2020	4.6 ± 0.8	
	Xinxiang	Jan–Feb 2020	4.8 ± 0.9	
	Puyang	Jan–Feb 2020	4.9 ± 0.9	
	Jiaozuo	Jan–Feb 2020	5.0 ± 0.8	
	Shangqiu	Jan–Feb 2020	4.6 ± 0.8	
	Nanyang	Jan–Feb 2020	4.3 ± 0.7	
Urban	Beijing	Jan–Feb 2015	4.5	[(Guo et al., 2017)]
	Beijing	Dec 2016	4.3 ± 0.4	[(Liu et al., 2017)]
	Beijing	Feb 2017	4.5 ± 0.7	[(Ding et al., 2019)]
	Tianjin	Dec-Jun 2015	4.9 ± 1.4	[(Shi et al., 2017)]
	Tianjin	Aug 2015	3.4 ± 0.5	[(Shi et al., 2019)]
	Hohhot	Winter	5.7	[(Wang et al., 2019)]
	Mt. Tai	Summer	2.9 ± 0.5	[(Liu et al., 2021)]
	Taoyuan	Nov 2017–Jan 2018	5.1 ± 1.0	[(Duan et al., 2021)]
	Zhengzhou	Jan 2018	4.5	[(Wang et al., 2020)]
	Anyang	Jan 2018	4.8	[(Wang et al., 2020)]
Mountain	Mt. Tai	Summer	3.6 ± 0.7	[(Liu et al., 2021)]
Rural	Shanglan	Nov 2017–Jan 2018	5.5 ± 1.1	[(Duan et al., 2021)]

References

Ding, J., Zhao, P., Su, J., Dong, Q., Du, X., and Zhang, Y.: Aerosol pH and its driving factors in Beijing, Atmos. Chem. Phys. 19, 7939 – 7954, https://doi.org/10.5194/acp-19-7939-2019, 2019.

Duan, X., Yan, Y., Peng, L., Xie, K., Hu, D., Li, R., and Wang, C.: Role of ammonia in secondary inorganic aerosols formation at an ammonia-rich city in winter in north China: A comparative study among industry, urban, and rural sites, Environ. Pollut., 291, 118151, https://doi.org/10.1016/j.envpol.2021.118151, 2021.

Feng, S., Xu, W., Cheng, M., Ma, Y., Wu, L., Kang, J., Wang, K., Tang, A., Collett, J. L., Fang, Y., Goulding, K., Liu, X., and Zhang, F.: Overlooked nonagricultural and wintertime agricultural NH_3 emissions in Quzhou county, North China Plain: evidence from ^{15}N-Stable Isotopes. Environ. Sci. Technol. Lett. 9, 127 – 133, https://doi.org/10.1021/acs.estlett.1c00935, 2022.

Gu, R., Zheng, P., Chen, T., Dong, C., Wang, Y. n., Liu, Y., Liu, Y., Luo, Y., Han, G., Wang, X., Zhou, X., Wang, T., Wang, W., and Xue, L.: Atmospheric nitrous acid (HONO) at a rural coastal site in North China: Seasonal variations and effects of biomass burning, Atmos. Environ., 229, https://doi.org/10.1016/j.atmosenv.2020.117429, 2020.

Guo, H., Weber, R. J., and Nenes, A.: High levels of ammonia do not raise fine particle pH sufficiently to yield nitrogen oxide-dominated sulfate production, Sci. Rep., 7, 12109, https://doi.org/10.1038/s41598-017-11704-0, 2017.

Hao, Q., Jiang, N., Zhang, R., Yang, L., and Li, S.: Characteristics, sources, and reactions of nitrous acid during winter at an urban site in the Central Plains Economic Region in China, Atmos. Chem. Phys. 20, 7087 – 7102, https://doi.org/10.5194/acp-20-7087-2020, 2020.

HOFZUMAHAUS, T. B. a.: Latitudinal variation of measured NO2 photolysis frequencies over the Atlantic Ocean between 50° N and 30° S., J. Atmos. Chem.

15, 269 – 282, https://doi.org/10.1007/bf00115398, 1992.

Hu, Q., Zhang, L., Evans, G. J., and Yao, X.: Variability of atmospheric ammonia related to potential emission sources in downtown Toronto, Canada, Atmos. Environ. 99, 365 – 373, https://doi.org/10.1016/j.atmosenv.2014.10.006, 2014.

Huang, R.-J., Yang, L., Cao, J., Wang, Q., Tie, X., Ho, K.-F., Shen, Z., Zhang, R., Li, G., Zhu, C., Zhang, N., Dai, W., Zhou, J., Liu, S., Chen, Y., Chen, J., and O'Dowd, C. D.: Concentration and sources of atmospheric nitrous acid (HONO) at an urban site in Western China, Sci. Total. Environ. 02, 165 – 172. https://doi.org/10.1016/j.scitotenv.2017.02.166, 2017.

Huy, D. H., Thanh, L. T., Hien, T. T., Noro, K., and Takenaka, N.: Characteristics of ammonia gas and fine particulate ammonium from two distinct urban areas: Osaka, Japan, and Ho Chi Minh City, Vietnam, Environ Environ. Sci. Pollut. Res. Int. 24, 8147 – 8163, https://doi.org/10.1007/s11356-017-8496-5, 2017.

Kramer, L. J., Crilley, L. R., Adams, T. J., Ball, S. M., Pope, F. D., and Bloss, W. J.: Nitrous acid (HONO) emissions under real-world driving conditions from vehicles in a UK road tunnel, Atmos. Chem. Phys. 20, 5231 – 5248, https://doi.org/10.5194/acp-20-5231-2020, 2020.

Liu, M., Song, Y., Zhou, T., Xu, Z., Yan, C., Zheng, M., Wu, Z., Hu, M., Wu, Y., and Zhu, T.: Fine particle pH during severe haze episodes in northern China, Geophys. Res. Lett. 44, 5213 – 5221, https://doi.org/10.1002/2017gl073210, 2017.

Liu, P., Zhao, X., Zhang, C., Chen, H., Wang, J., Xue, L., Chen, J., and Mu, Y.: Fine particle pH and its influencing factors during summer at Mt. Tai: Comparison between mountain and urban sites, Atmos. Environ., 261, https://doi.org/10.1016/j.atmosenv.2021.118607, 2021.

Liu, Y., Ni, S., Jiang, T., Xing, S., Zhang, Y., Bao, X., Feng, Z., Fan, X., Zhang, L., and Feng, H.: Influence of Chinese New Year overlapping COVID-19 lockdown on HONO sources in Shijiazhuang, Sci. Total Environ., 745, 141025,

https://doi.org/10.1016/j.scitotenv.2020.141025, 2020a.

Liu, Y., Zhang, Y., Lian, C., Yan, C., Feng, Z., Zheng, F., Fan, X., Chen, Y., Wang, W., Chu, B., Wang, Y., Cai, J., Du, W., Daellenbach, K. R., Kangasluoma, J., Bianchi, F., Kujansuu, J., Petäjä, T., Wang, X., Hu, B., Wang, Y., Ge, M., He, H., and Kulmala, M.: The promotion effect of nitrous acid on aerosol formation in wintertime in Beijing: the possible contribution of traffic-related emissions, Atmos. Chem. Phys. 20, 13023 – 13040, https://doi.org/10.5194/acp-20-13023-2020, 2020b.

Lv, S., Wang, F., Wu, C., Chen, Y., Liu, S., Zhang, S., Li, D., Du, W., Zhang, F., Wang, H., Huang, C., Fu, Q., Duan, Y., and Wang, G.: Gas-to-aerosol phase partitioning of atmospheric water-soluble organic compounds at a rural site in China: an enhancing effect of NH_3 on SOA formation. Environ. Sci. Technol. 56, 3915 – 3924, https://doi.org/10.1021/acs.est.1c06855, 2022.

Mikuska, P., Motyka, K., and Vecera, Z.: Determination of nitrous acid in air using wet effluent diffusion denuder–FIA technique, Talanta; 77, 635 – 641, https://doi.org/10.1016/j.talanta.2008.07.008, 2008.

Rumsey, I. C., Cowen, K. A., Walker, J. T., Kelly, T. J., Hanft, E. A., Mishoe, K., Rogers, C., Proost, R., Beachley, G. M., Lear, G., Frelink, T., and Otjes, R. P.: An assessment of the performance of the Monitor for aerosols and gases in ambient air (MARGA): a semi-continuous method for soluble compounds. Atmos. Chem. and Phys. 14, 5639 – 5658, https://doi.org/10.5194/acp-14-5639-2014, 2014.

Saraswati, Sharma, S. K., Saxena, M., and Mandal, T. K.: Characteristics of gaseous and particulate ammonia and their role in the formation of secondary inorganic particulate matter at Delhi, India, Atmos. Res. 218, 34 – 49, https://doi.org/10.1016/j.atmosres.2018.11.010, 2019.

Seinfeld, J. H., Pandis, S. N., and Noone, K. J.: Atmospheric chemistry and physics: from air pollution to climate change. Phys. Today 51, 88 – 90, https://doi.org/10.1063/1.882420, 1998.

Shi, G., Xu, J., Peng, X., Xiao, Z., Chen, K., Tian, Y., Guan, X., Feng, Y., Yu, H., Nenes, A., and Russell, A. G.: pH of pH of aerosols in a polluted atmosphere: source contributions to highly acidic aerosol. Environ. Sci. Technol. 51, 4289 – 4296, https://doi.org/10.1021/acs.est.6b05736, 2017.

Shi, G., Xu, J., Shi, X., Liu, B., Bi, X., Xiao, Z., Chen, K., Wen, J., Dong, S., Tian, Y., Feng, Y., Yu, H., Song, S., Zhao, Q., Gao, J., and Russell, A. G.: Aerosol pH dynamics during haze periods in an urban environment in China: use of detailed, hourly, speciated observations to study the role of ammonia availability and secondary aerosol formation and urban environment. J. Geophys. Res. Atmos. 124, 9730 – 9742, https://doi.org/10.1029/2018jd029976, 2019.

Song, S., Gao, M., Xu, W., Shao, J., Shi, G., Wang, S., Wang, Y., Sun, Y., and McElroy, M. B.: Fine-particle pH for Beijing winter haze as inferred from different thermodynamic equilibrium models, Atmos. Chem. and Phys. 18, 7423 – 7438, https://doi.org/10.5194/acp-18-7423-2018, 2018.

Takeuchi M, M. Y., Tsunoda H, Tanaka H.: Atmospheric acid gases in tokushima, Japan, monitored with parallel plate wet denuder coupled ion chromatograph. Anal. Sci. 29, 165 – 168, https://doi.org/10.2116/analsci.29.165, 2013.

Trebs, I., B. B., C. A., U. Rummel, M. Blumthaler, R. K. O., F. X. M., S. F., a., and Andreae., M. O.: Relationship between the NO2 photolysis frequency and the solar. Atmos. Meas. Tech. 2, 725 – 739, https://doi.org/10.5194/amt-2-725-2009, 2009.

VandenBoer, T. C., Markovic, M. Z., Sanders, J. E., Ren, X., Pusede, S. E., Browne, E. C., Cohen, R. C., Zhang, L., Thomas, J., Brune, W. H., and Murphy, J. G.: Evidence for a nitrous acid (HONO) reservoir at the ground surface in Bakersfield, CA, during CalNex 2010. J. Geophys. Res. Atmos. 119, 9093 – 9106, https://doi.org/10.1002/2013jd020971, 2014.

Wang, G., Zhang, R., Gomez, M. E., Yang, L., Levy Zamora, M., Hu, M., Lin, Y., Peng, J., Guo, S., Meng, J., Li, J., Cheng, C., Hu, T., Ren, Y., Wang, Y., Gao, J.,

385 Cao, J., An, Z., Zhou, W., Li, G., Wang, J., Tian, P., Marrero-Ortiz, W., Secrest, J.,
386 Du, Z., Zheng, J., Shang, D., Zeng, L., Shao, M., Wang, W., Huang, Y., Wang, Y.,
387 Zhu, Y., Li, Y., Hu, J., Pan, B., Cai, L., Cheng, Y., Ji, Y., Zhang, F., Rosenfeld, D.,
388 Liss, P. S., Duce, R. A., Kolb, C. E., and Molina, M. J.: Persistent sulfate
389 formation from London Fog to Chinese haze. Proc. Natl. Acad. of Sci. U. S. A.
390 113, 13630 – 13635, https://doi.org/10.1073/pnas.1616540113, 2016a.
391 Wang, H., Ding, J., Xu, J., Wen, J., Han, J., Wang, K., Shi, G., Feng, Y., Ivey, C. E.,
392 Wang, Y., Nenes, A., Zhao, Q., and Russell, A. G.: Aerosols in an arid
393 environment: the role of aerosol water content, particulate acidity, precursors,
394 and relative humidity on secondary inorganic aerosols. Sci. Total Environ. 646,
395 564 – 572, https://doi.org/10.1016/j.scitotenv.2018.07.321, 2019.
396 Wang, R., Ye, X., Liu, Y., Li, H., Yang, X., Chen, J., Gao, W., and Yin, Z.:
397 Characteristics of atmospheric ammonia and its relationship with vehicle
398 emissions in a megacity in China, Atmos. Environ. 182, 97 – 104,
399 https://doi.org/10.1016/j.atmosenv.2018.03.047, 2018.
400 Wang, S., Wang, L., Li, Y., Wang, C., Wang, W., Yin, S., and Zhang, R.: Effect of
401 ammonia on fine-particle pH in agricultural regions of China: comparison
402 between urban and rural sites, Atmos. Chem. Phys. 20, 2719 – 2734,
403 https://doi.org/10.5194/acp-20-2719-2020, 2020.
404 Wang, S., Fan, X., Xu, Y., Zhang, R., and Ren, B.: Insight into the non-linear
405 responses of particulate sulfate to reduced SO_2 concentration: A perspective from
406 the aqueous-phase reactions in a megacity in Northern China, Atmos. Res., 290,
407 https://doi.org/10.1016/j.atmosres.2023.106796, 2023.
408 Wang, W., Wang, S., Xu, J., Zhou, R., Shi, C., and Zhou, B.: Gas-phase ammonia and
409 $PM_{2.5}$ ammonium in a busy traffic area of Nanjing, China, Environ. Sci. Pollut.
410 Res. Int., 23, 1691 – 1702, https://doi.org/10.1007/s11356-015-5397-3, 2016b.
411 Wang, X., Yin, S., Zhang, R., Yuan, M., and Ying, Q.: Assessment of summertime O_3
412 formation and the O_3-NO_X-VOC sensitivity in Zhengzhou, China using an

observation-based model. Sci. Total Environ. 813, 152449, https://doi.org/10.1016/j.scitotenv.2021.152449, 2022.

Wang, Y., Zhu, S., Ma, J., Shen, J., Wang, P., Wang, P., and Zhang, H.: Enhanced atmospheric oxidation capacity and associated ozone increases during COVID-19 lockdown in the Yangtze River Delta, Sci. Total Environ., 768, 144796, https://doi.org/10.1016/j.scitotenv.2020.144796, 2021.

Wu, S., Zhang, Y., Schwab, J., Li, Y., Liu, Y., and Yuan, C.: High-resolution ammonia emissions inventories in Fujian, China, 2009–2015, Atmos. Environ., 162, 100 – 114, https://doi.org/10.1016/j.atmosenv.2017.04.027, 2017.

Xu, W., Kuang, Y., Zhao, C., Tao, J., Zhao, G., Bian, Y., Yang, W., Yu, Y., Shen, C., Liang, L., Zhang, G., Lin, W., and Xu, X.: NH_3-promoted hydrolysis of NO2 induces explosive growth in HONO, Atmos. Chem. Phys. 19, 10557 – 10570, https://doi.org/10.5194/acp-19-10557-2019, 2019.

Xuan, H., Zhao, Y., Ma, Q., Chen, T., Liu, J., Wang, Y., Liu, C., Wang, Y., Liu, Y., Mu, Y., and He, H.: Formation mechanisms and atmospheric implications of summertime nitrous acid (HONO) during clean, ozone pollution and double high-level $PM_{2.5}$ and O_3 pollution periods in Beijing. Sci. Total Environ. 857: 159538, https://doi.org/10.1016/j.scitotenv.2022.159538, 2023.

Zhao, Y., Zhang, N., Wei, Q., Han, Y., Mao, K., Cai, Y., Li, R.: Flow injection chemiluminescence method in analytical chemistry. Spectrosc. Spectral. Analys. 30, 2512 – 2517, https://doi.org/10.3964/j.issn.1000-0593(2010)09-2512-06, 2010.

Yu, Y., Cheng, P., Li, H., Yang, W., Han, B., Song, W., Hu, W., Wang, X., Yuan, B., Shao, M., Huang, Z., Li, Z., Zheng, J., Wang, H., and Yu, X.: Budget of nitrous acid (HONO) at an urban site in the fall season of Guangzhou, China, Atmos. Chem. Phys. 22, 8951 – 8971, https://doi.org/10.5194/acp-22-8951-2022, 2022.

Zhang, W., Tong, S., Jia, C., Wang, L., Liu, B., Tang, G., Ji, D., Hu, B., Liu, Z., Li, W., Wang, Z., Liu, Y., Wang, Y., and Ge, M.: Different HONO sources for three

layers at the urban area of Beijing. Environ. Sci. Technol. 54, 12870 – 12880, https://doi.org/10.1021/acs.est.0c02146, 2020a.

Zhang, Y., Liu, X., Fang, Y., Liu, D., Tang, A., and Collett, J. L.: Atmospheric ammonia in Beijing during the COVID-19 outbreak: concentrations, sources, and implications. Environ. Sci. Technol. Lett. 8, 32 – 38, https://doi.org/10.1021/acs.estlett.0c00756, 2020b.